Article

Unusual Organization of I-BAR Proteins on Tubular and Vesicular Membranes

Zack Jarin,[1] Feng-Ching Tsai,[2,3] Aram Davtyan,[4] Alexander J. Pak,[4] Patricia Bassereau,[2,3] and Gregory A. Voth[4,*]

[1]Pritzker School for Molecular Engineering, The University of Chicago, Chicago, Illinois; [2]Laboratoire Physico Chimie Curie, Institut Curie, PSL Research University, CNRS UMR168, Paris, France; [3]Sorbonne Universités, UPMC University Paris 06, Paris, France; and [4]Department of Chemistry, Chicago Center for Theoretical Chemistry, The James Franck Institute, and Institute for Biophysical Dynamics, The University of Chicago, Chicago, Illinois

ABSTRACT Protein-mediated membrane remodeling is a ubiquitous and critical process for proper cellular function. Inverse Bin/Amphiphysin/Rvs (I-BAR) domains drive local membrane deformation as a precursor to large-scale membrane remodeling. We employ a multiscale approach to provide the molecular mechanism of unusual I-BAR domain-driven membrane remodeling at a low protein surface concentration with near-atomistic detail. We generate a bottom-up coarse-grained model that demonstrates similar membrane-bound I-BAR domain aggregation behavior as our recent Mesoscopic Membrane with Explicit Proteins model. Together, these models bridge several length scales and reveal an aggregation behavior of I-BAR domains. We find that at low surface coverage (i.e., low bound protein density), I-BAR domains form transient, tip-to-tip strings on periodic flat membrane sheets. Inside of lipid bilayer tubules, we find linear aggregates parallel to the axis of the tubule. Finally, we find that I-BAR domains form tip-to-tip aggregates around the edges of membrane domes. These results are supported by in vitro experiments showing low curvature bulges surrounded by I-BAR domains on giant unilamellar vesicles. Overall, our models reveal new I-BAR domain aggregation behavior in membrane tubules and on the surface of vesicles at low surface concentration that add insight into how I-BAR domain proteins may contribute to certain aspects of membrane remodeling in cells.

SIGNIFICANCE Our study aims to understand inverse Bin/Amphiphysin/Rvs (I-BAR) protein organization at realistic lower surface coverage before large-scale deformation and how existing global curvature affects organization. First, we model I-BAR protein assembly on tubular and vesicular membranes using coarse-grained models. Our separate bottom-up and top-down models both show that I-BAR domains form local deformations that couple to the global membrane curvature to form long axial aggregates tubules and end-to-end rings on small vesicles. Second, we observe novel membrane remodeling behavior of the I-BAR domain of IRSp53 in in vitro fluorescence experiments showing that the I-BAR domain forms rings around lipid bilayer deformations. Together, we experimentally observe a new I-BAR-driven remodeling phenomenon on vesicles and provide a potential explanation using our coarse-grained models.

INTRODUCTION

The cell membrane is composed of a variety of lipids, proteins, and small molecules and creates a barrier between the inner workings of the cell and the extracellular matrix. This complex barrier is a highly dynamic surface that typically prefers to be locally flat. Throughout many biological processes, large deformations are required, and peripheral membrane proteins facilitate this ubiquitous process. A variety of proteins bind to the membrane and generate

membrane curvature. One such family of proteins that cause large-scale deformation through cooperative action is the Bin/Amphiphysin/Rvs (BAR) domain superfamily. BAR domains are banana-shaped homodimers known to bind to lipid bilayers and generate curvature through electrostatic interactions and, in some cases, amphipathic helical insertions into the membrane (1–3). BAR domains have diverse functionality because each member of the superfamily generates a variety of positive or negative curvatures.

IRSp53 is a member of the inverse BAR (I-BAR) domain family of the BAR domain superfamily. These proteins generate negative principal curvature and are key to the formation of cellular protrusions (e.g., filopodia) (4–7). I-BAR domains are proposed to act through a scaffolding

---

mechanism that generates local curvature on lipid membranes, leading to I-BAR domain aggregation and subsequent formation of microns-long protrusions (8–11). Interestingly, in vitro experimental data regarding the I-BAR domain of IRSp53 have indicated a preference for low curvature commensurate with its intrinsic curvature (12). The aggregation and collective behavior that drives membrane deformations, and potentially gives rise to sorting in membrane tubules, is therefore of significant biological interest.

I-BAR domains have been the subject of several computational and theoretical studies (13–17), with varying degrees of accuracy. I-BAR domain-mediated membrane remodeling spans many length scales, from nanometer-scale local interactions between individual I-BAR domains and lipid headgroups to the micron-scale deformations collectively induced by many I-BAR domains. The multiscale nature of membrane remodeling has led to a range of studies from recent atomistic simulations exploring the behavior of small I-BAR domains with relatively high accuracy to simulations modeling the collective effects of tens of I-BAR domains at the mesoscale. However, these previous studies lack the connection and correspondence between the two scales; this disparity could result in coarse-grained (CG) or mesoscopic models that are inconsistent with atomistic simulations (18). For example, CG simulations can assume that membrane-bound I-BAR domains have the same intrinsic curvature as the crystal structure, but recent all-atom simulations show that the curvature of an I-BAR domain decreases (i.e., I-BAR domain flattens) when bound to the membrane (17). Assumptions like this can cause disagreement between the all-atom and CG resolutions, resulting in different mechanisms of membrane remodeling.

Here, we use a multiscale approach combining CG and mesoscopic models (specifically, Mesoscopic Membrane with Proteins (19) [MesM-P]) to understand the organization of I-BAR domains on membranes of various geometries (18). This multiscale approach is uniquely suited to capture protein-mediated membrane remodeling because it incorporates the interplay between near nanometer to several micron-length scales. Broadly speaking (18), CG models can be derived from finer resolution, atomistic simulations (bottom-up), or by specifically reproducing experimental observables (top-down). Here, the former approach is adopted such that our protein CG model reproduces structural fluctuations observed in atomistic simulations, whereas our lipid CG model recapitulates the properties of a representative lipid bilayer membrane. Additionally, the MesM-P model, which is a lower resolution than the CG model, can be used to simulate significantly larger systems while remaining consistent with the membrane-bound protein aggregation behavior of our CG model. Together, these models span near atomistic to mesoscopic length scales, and the agreement of the two models (parameterized using separate methodologies) indicates the robustness of the CG phenomena we observe. We apply these models to understand the aggregation behavior of I-BAR domains on flat sheets that mimic the surface of giant unilamellar vesicles (GUVs), membrane tubules, and spherical membrane vesicles. We focus primarily on lower density surface coverage.

Our results show that both I-BAR domain models form local membrane troughs on flat sheets, and when I-BAR domains are on membranes with global curvature, the I-BAR domains orient to minimally perturb the membrane. We predict tip-to-tip string aggregates in tubule-shaped membranes and rings at the base of bulges on the surface of vesicles. Although the CG lipid and MesM-P models bear some differences, the behavior observed using the two models (each consistent with biologically relevant properties) is qualitatively similar. Both models show qualitatively similar behavior on surfaces with positive Gaussian curvature, providing a consistent mechanism for the formation of novel, low curvature deformations surrounded by I-BAR domains on GUVs.

MATERIALS AND METHODS

CG model details

The model consists of two components: a highly CG lipid bilayer and a CG IRSp53 I-BAR domain as shown in Fig. 1 A. The highly CG lipid bilayer was parameterized using a hybrid multiscale coarse-graining approach. The hybrid parameterization supplemented multiscale coarse-graining forces from atomistic simulations with analytical CG potentials to describe the short-range interactions, which has been described previously (20). The CG model was simulated in the Large-scale Atomic/Molecular Massively Parallel Simulator simulation engine (21).

The CG IRSp53 I-BAR domain model was parameterized from atomistic simulation to reproduce the atomistic structure fluctuations (e.g., intrinsic curvature fluctuations), which we expect to be critical to the membrane remodeling process. The atomistic simulations were composed of a lipid bilayer, IRSp53 I-BAR domain (Protein Data Bank: 2YKT (22)), and water using the CHARMM36 force field (23–25). The initial configuration of the membrane was first generated from Chemistry at Harvard Macromolecular Mechanics – Graphical User Interface (26–30) and equilibrated using the corresponding scheme and the Groningen Machine for Chemical Simulations simulation engine (31). The membrane was composed of 75% 1,2-dioleoyl-sn-glycero-3-phosphocholine, 20% 1,2-dioleoyl-sn-glycero-3-phosphoserine, and 5% phosphatidylinositol-4,5-diphosphate (PI(4,5)P$_2$). Then, the I-BAR domain was added to the simulation cell, and the hydration layer was increased with 150 mM NaCl using Groningen Machine for Chemical Simulations tools (31). The I-BAR domain was simulated with the membrane for 300 ns, and the final 100 ns were used to determine the mapping and parameterization of intraprotein forces. The map from atomistic to CG was found using essential dynamics coarse-graining (32), which divides the protein along its primary sequence. The essential dynamics coarse-graining protocol map is determined by finding divisions in the primary sequence that preserve the dynamics of the protein (i.e., the large amplitude motions within a CG bead are minimized, and the motion between beads are maximized). The divisions in the primary sequence are given in the Supporting Materials and Methods. Effective harmonic potentials were used for intraprotein interactions, with the parameters determined using a heterogeneous elastic network model (33). The spring constants and equilibrium distances are fit to reproduce the mapped structure and fluctuations from an atomistic molecular dynamics trajectory and are provided in the Supporting Materials and Methods.
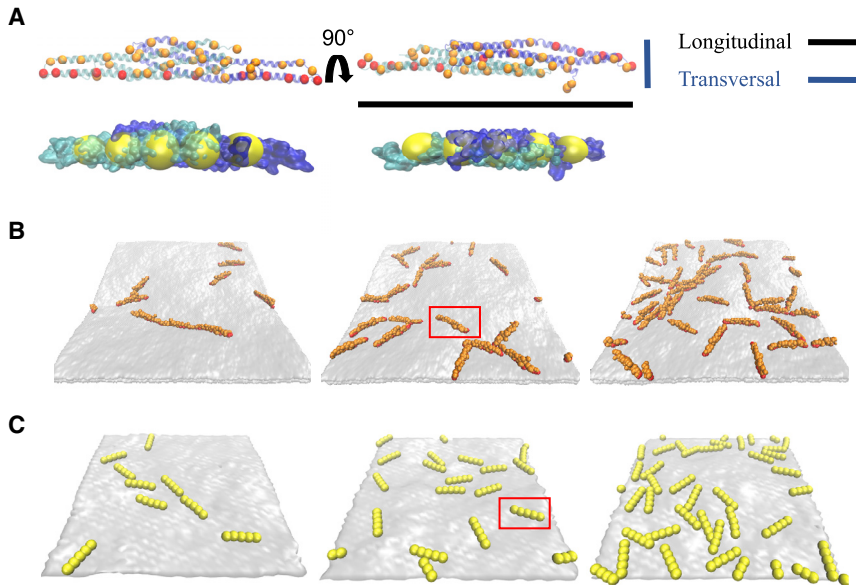
FIGURE 1 Side-by-side image of CG and MesM-P models, snapshots of flat sheet configurations. (*A*) Shown are the side (*left*) and top (*right*) view of an overlay of CG I-BAR domain (*orange*, *red*) and the secondary structure of each monomer (*cyan* and *blue*) and an overlay of MesM-P I-BAR domain (*yellow*) and a space filling representation of each monomer. The attractive and excluded volume CG beads colored in red and orange, respectively, are shown, along with the definition of the longitudinal and transversal dimensions of the I-BAR domain. (*B*) Shown is a snapshot of 5, 10, and 20% coverage of a 100 nm by 100 nm flat sheet with single I-BAR domain highlighted with a red box. (*C*) Shown are MesM-P snapshots of 5, 10, and 20% coverage of a 100 nm by 100 nm with a single I-BAR domain highlighted with a red box. To see this figure in color, go online.

The direct protein-protein interactions were purely repulsive to capture the excluded volume of each I-BAR domain. Additional screened electrostatic interactions between I-BAR domains were investigated in the Supporting Materials and Methods and reinforce the aggregation behavior due to purely membrane-mediated attraction. The effective potential between the CG beads of the protein and the headgroup beads of the CG lipids was modeled as a 10-6 shifted force Lennard-Jones potential (34). At the CG resolution, the effective potential between the protein and lipid membrane is, by its nature, a simplification of the complex electrostatic interactions at the atomistic protein-membrane interface and is meant to capture the local membrane deformation driven by an isolated, atomistically resolved I-BAR domain (17). As further mechanistic studies of local membrane deformation by I-BAR domains are performed, the CG interactions could be refined to better reproduce the complex nature of membrane remodeling. Without an exhaustive study of I-BAR domain membrane remodeling at a finer resolution, the effective attraction strength was taken as a parameter, and its effect on local deformation was quantified by a comparison to previous atomistic simulations (17).

Mesoscopic membrane simulations with explicit proteins

Here, we used a reduced and scaled-down version of the recent MesM-P model (19) that relies on a discretized formulation of membrane elastic theory (35). In the original model, the membrane is represented as a collection of quasiparticles ∼7 nm in diameter. Each quasiparticle describes a patch of lipid bilayer given its position and momentum with additional scalar fields to represent local protein concentration and lipid composition. As a result, MesM-P allows for efficient modeling of large-scale membrane shape changes, protein binding and unbinding, and their interplay on nearly experimental length and timescales (19).

In this work, we use only the elastic component of the MesM-P model that describes three-dimensional membrane undulations and bending (i.e., without using mesoscopic solvent or implicit variables describing the local protein concentration and lipid composition). Instead, we use an approach similar to the CG model and include explicit very highly CG representations of I-BAR proteins, which are modeled as five-bead linear chains with varied sizes shown in Fig. 1 *A*. The size variation of the beads is included to, in part, reproduce the shape of an I-BAR domain. For the membrane, we also use smaller sized beads of ∼3 nm, which is consistent with the width of I-BAR. We have used Lennard-Jones-like shifted force

4-2 potentials for membrane-protein interactions with various strengths (34). The MesM-P model was simulated in the Large-scale Atomic/Molecular Massively Parallel Simulator simulation engine (21).

The final set of simulations utilizes a guiding potential to replicate membrane configurations seen in the in vitro experiments. The flower petal structure in the latter (see Results) is likely caused by I-BAR domain-driven membrane remodeling. This full phenomenon is not observable with the MesM-P model due to the use of periodic boundaries to describe the surface of a GUV. Instead, the flat sheet is deformed using a spherical guiding potential. The membrane is initially flat, and the guiding potential is moved toward the surface to create a membrane deformation similar to the deformations made by CG I-BAR domains on small vesicles and the accompanying in vitro experiments.

More details and the parameters of each computational model are given in the Supporting Materials and Methods.

Reagents

Total brain lipid extract (131101P), brain L-α-PI(4,5)P$_2$ (840046P), and 1,2-distearoyl-*sn*-glycero-3-phosphoethanolamine-N-[biotinyl(polyethyleneglycol)-2000] (880129P) were purchased from Avanti Polar Lipids (Alabaster, AL). BODIPY-TR-C5-ceramide, (BODIPY-TR ceramide, D7540), BODIPYFL C5-hexadecanoyl phosphatidylcholine (D3803), and Alexa Fluor 488 (AX488) C5-Maleimide were purchased from Invitrogen (Carlsbad, CA). GloPIPs BODIPY TMR-PtdIns(4,5)P2, C16 (C45M16a) was purchased from Echelon Biosciences (Salt Lake City, UT). β-Casein from bovine milk (>98% pure, C6905) and other reagents were purchased from Sigma-Aldrich (St. Louis, MO).

Protein purification and labeling

Recombinant mouse IRSp53 I-BAR domain was purified and labeled with AX488 dyes as previously described (9).

GUVs preparation and observation

For all experiments, GUVs composed of brain total lipid extract (36) supplemented with 5 mole percentage (mol%) brain PI(4,5)P$_2$, 0.2 mol% 1,2-distearoyl-*sn*-glycero-3-phosphoethanolamine-N-[biotinyl(polyethyleneglycol)-2000], and 0.5 mol% BODIPY-TR ceramide

were prepared by electroformation on platinum electrodes overnight at 4°C in a physiologically relevant salt buffer. The salt buffer outside GUVs was 20 mM Tris (pH 7.5), 60 mM NaCl, and 100 mM sucrose. The salt buffer inside GUVs was 20 mM Tris (pH 7.5), 60 mM NaCl, and 100 mM glucose.

GUVs were incubated with IRSp53 I-BAR domain at a bulk concentration of 0.02–0.1 μM for at least 30 min at room temperature before observation. For all experiments, microscope slides and coverslips were washed with water and ethanol followed by passivation with a β-casein solution at a concentration of 5 mg/mL for at least 5 min at room temperature. GUVs were observed by Nikon Eclipse Ti microscope (Nikon, Tokyo, Japan) equipped with Yokogawa CSU-X1 confocal head, 100× CFI Plan Apo VC objective (Nikon), and QuantEM:512SC camera (Photometrics, Tucson, AZ).

RESULTS

Planar membranes

First, we compared the two modeling approaches by separate simulations of both I-BAR domain models on tension-free, periodic flat lipid bilayers at various I-BAR protein surface densities. Infinite flat sheets are a close approximation to the surface of GUVs that have quasinull local curvature. The CG and MesM-P simulations demonstrated a preference for forming relatively linear aggregates, as shown in Fig. 1, B and C, respectively.

At low surface coverage, transient short linear strings of I-BAR form in both the CG and MesM-P models (Fig. 1). As surface coverage increases from 5 to 20%, the transient linear strings change into crowded strings in which each I-BAR domain of the linear aggregate can switch orientation from one neighbor to another. We observe comparable behavior in both models, indicating our results are robust with respect to model resolution.

Next, we investigated the effects of protein-lipid interaction on protein organization and curvature generated. The effective protein-lipid interaction be changed in an in vitro experiment by changing the local concentration of negatively charged lipids or phosphoinositides. Fig. 2 shows final protein configurations using a constant coverage of 10% as a function of protein-lipid interaction strengths. In Fig. 2, we observe that at increased protein-lipid interactions strength, significantly more curvature is generated, and linear aggregates are much more likely to form. It is reasonable to expect that, as the local curvature increases, the subsequent aggregation also increases, given the nature of membrane-mediated protein interactions (37). In the CG models parameterized here, membrane-mediated interactions between proteins can broadly be defined as effective protein interactions caused by perturbations to the membrane after protein binding events. The response of the membrane to protein binding (e.g., induced curvature or dampened fluctuations) results in an effective protein interaction that drives membrane aggregation (38,39). In fact, we demonstrate here that membrane-mediated interactions are sufficient for protein aggregation (40–42).

We calculated the mean principal curvature generated on the x and y axes for each model to further quantify the effects of interaction strength on I-BAR domain organization. Both models exhibit curvature parallel and perpendicular to the longitudinal axis of the I-BAR domain (see Fig. 1 A). In the presence of thermal fluctuations, deformation along either axis results in transient Gaussian curvature and variations in the principal curvature. Plots of mean principal curvature are shown in Fig. 2 B, corresponding to the snapshots of Fig. 2 A. With weak protein-lipid interactions, we see little to no aggregation, and the I-BAR domains are disordered. With intermediate interactions, we find that there are linear aggregates and the mean curvature driven by isolated I-BAR domains to be around 0–0.5 10^{-1}/nm, similar to the curvature observed near a single I-BAR domain in atomistic simulations (17). With stronger protein-lipid interactions, we observed complete linear aggregate formation and significantly more membrane deformation than atomistic simulation of isolated I-BAR domains, which is to be expected. The local membrane deformation is crucial to understanding I-BAR domain curvature sensing, and so in the following sections, we address how globally curved surfaces affect the aggregation of I-BAR domains.

A

B
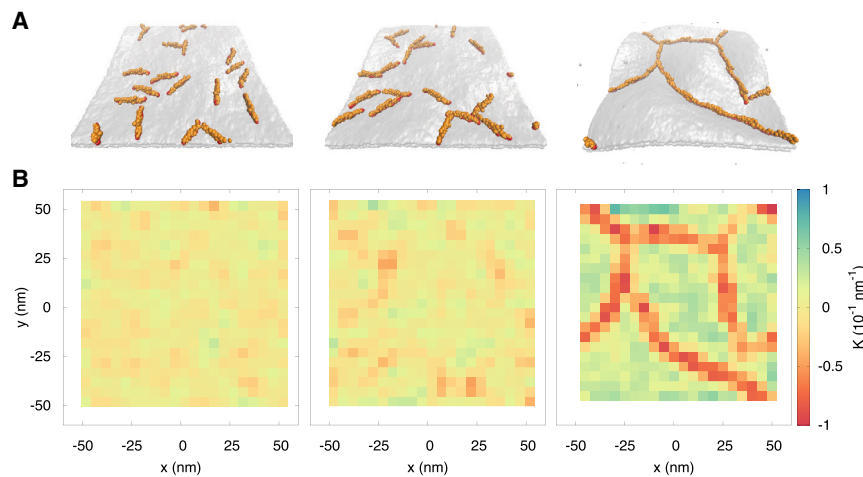
FIGURE 2 Effect of I-BAR-lipid interaction strength on local membrane curvature generation at 10% coverage. (A) Shown are snapshots of CG model with increasing interaction strength between attractive I-BAR CG beads and lipid head bead. From left to right: the strengths increase from 0.5, 1.0, to 1.5 kcal/mol. (B) Mean curvature was calculated as a function of the position on the membrane for the snapshots in (A). To see this figure in color, go online.

Tubular membranes

We mimicked the experimental conditions of Prévost et al. (12) by simulating each I-BAR domain model inside of a membrane tubule. In the experiments, tubules are formed by pulling on a micropipette-aspirated GUV using optical tweezers, with the curvature of the tubule controlled using the applied pressure in the pipette. In the tubule simulations, the surface tension is initially zero as the radius and length of the tubule are allowed to equilibrate before I-BAR domains are introduced to the system and, subsequently, bind to the lipid bilayer. After this initial equilibration, the length of the tubule is then held constant with the radius allowed to fluctuate as we seek to understand I-BAR organization in tubules pulled from GUVs, which are not tension free.

To understand the nature of the curvature-sorting property of the I-BAR domain, we probed the I-BAR domain organization inside tubules with two different radii. Interestingly, CG simulations at these lower surface coverages produced rather linear aggregates of I-BAR along the major axis of the tubule (Fig. 3). We quantified the ordering between proteins by plotting the probability density of the order parameter, $S = (3\cos^2\theta - 1)/2$, where θ is the angle formed between the long dimension of two I-BAR domains. The bimodal probability densities indicate that perpendicular ($S = -0.5$) and parallel ($S = 1$) aggregates are extremely prevalent, as shown in Fig. 3 E. As the tubule radius is increased from 25 to 50 nm, however, we noticed an increased stability of the perpendicular aggregates. The increased stability of parallel aggregates in the narrower tubule is likely due to the coupling between the curvature generated by each I-BAR domain and the inherent curvature of the tubule itself. We quantified ordering due to tubule radius by plotting the probability of the linearity shown in Fig. 3 F. Linearity is defined as the cosine of the angle formed by each I-BAR domain and the axis of the tubule (i.e., the z axis). Linearity is 0 when the protein is
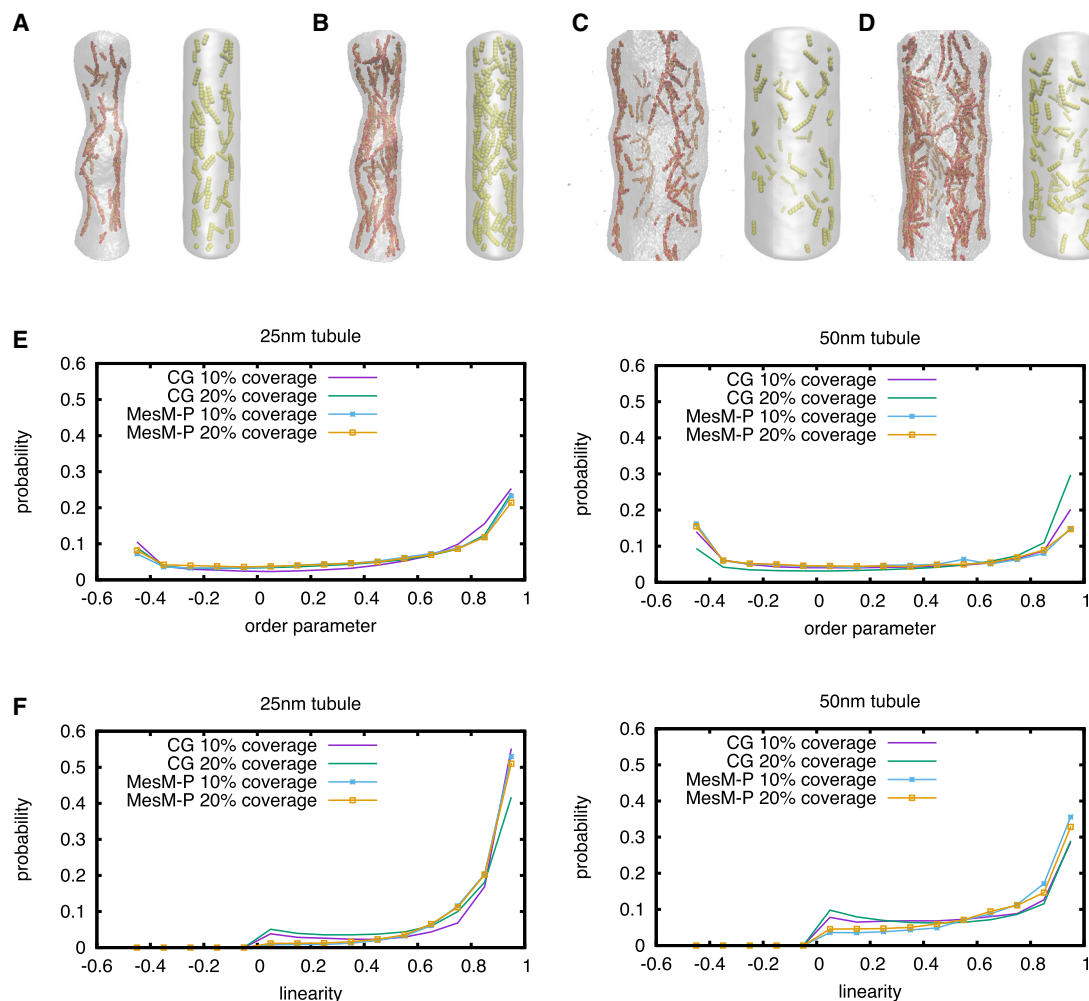
FIGURE 3 Tubule snapshots and time series of ordering with the z axis. (A) Shown is 10% and (B) 20% coverage in a periodic ~25-nm radius tubules and (C) 10% and (D) 20% surface coverage in a ~50-nm radius tubule (left CG snapshots, right MesM-P snapshots). (E) Shown is a normalized histogram of order parameter for various bound densities and tubule radii. (F) Shown is a normalized histogram of cosine of the angle formed by a single protein and the z axis for various bound densities and tubule radii. To see this figure in color, go online.

perpendicular to the axis of the tubule and 1 when parallel to the axis. Fig. 3 F shows that the protein has a significant preference for the axial direction in the narrower tubules (i.e., perpendicular or spiral aggregates are less likely as I-BAR domains prefer axial aggregation). Axial aggregates are preferential because CG I-BAR domains form local membrane troughs, and the axial orientation requires less membrane deformation than the perpendicular direction. In other words, the trough formed by a single I-BAR domain is more stable when formed in the axial direction, and as I-BAR domains aggregate, they are already axially aligned.

Spherical membranes

We investigated surfaces with global Gaussian curvature to understand how I-BAR protein bind and induce large-scale deformation. Considering the limits and boundary conditions of the two simulation models, we used two separate approaches to approximate the surface of a GUV; we simulated a small CG vesicle of 200-nm diameter and a large MesM-P sheet with the curvature driven by a guiding potential. The approximations made here are necessary to construct simulations that are more computationally tractable than a complete GUV. These simulations test the stability of both linear I-BAR aggregates on surfaces that display positive Gaussian curvature.

The aggregation behavior of CG I-BAR shows significant deformation of the surface of small vesicles surrounded by I-BAR domains. The linear aggregates form strings on the membrane and form bulges out of the membrane with I-BAR on the periphery. Next, we employed the MesM-P-based approach, which used a guiding potential (see Supporting Materials and Methods) to drive Gaussian curvature, and the organization of I-BAR domains is investigated. These simulations probe the aggregation behavior on the surface of a deformed vesicle with quasinull local curvature. When the membrane is perturbed into a ~325-nm diameter dome structure with a spherical guiding potential, I-BAR domains preferentially sort to the edge of the surface, forming a tip-to-tip ring as shown in Fig. 4 B. The preference for a tip-to-tip ring can be understood again as a way for the I-BAR domains to lie in a membrane trough; the edge of the dome structure is the region of the membrane that requires minimal perturbation to form a trough.

Experimental results

Finally, we experimentally studied the I-BAR-driven protein-membrane deformations on a GUV using fluorescence microscopy. We found that upon binding to phosphatidylinositol 4,5-biphosphate-containing GUVs, IRSp53 I-BAR domain deforms the GUV membranes into tubular invaginations toward the interior of the GUVs, where the I-BAR domain decorates the inner surface of the tubules (Fig. 5, A and C), as previously reported (9,43). The bulk of the I-BAR domain fluorescence, as seen in the maximal projections in
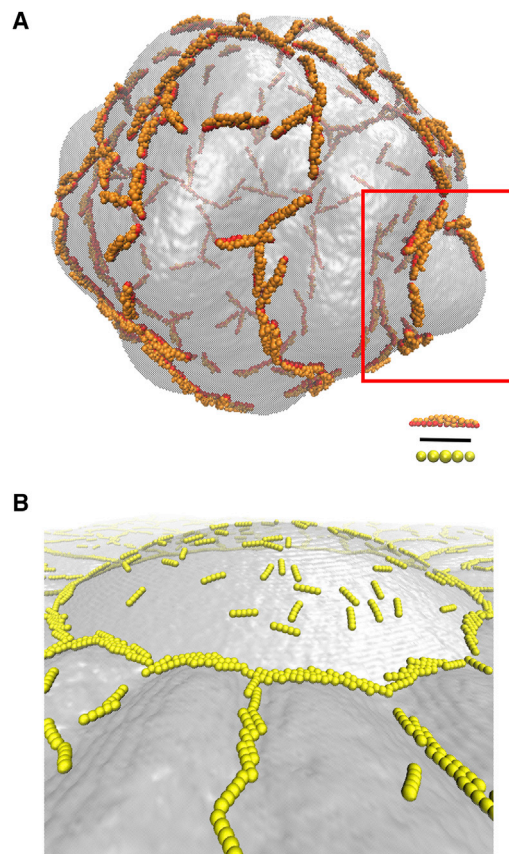
FIGURE 4 Curved membrane snapshots. (A) Shown is CG organization on a 200-nm diameter vesicle at ~10% coverage. In the red box, liner aggregates of I-BAR domain organized around the base of a membrane bulge are shown. (B) Shown is MesM-P organization around a ~325-nm diameter dome at ~10% coverage. Black scale bar represents 15 nm. To see this figure in color, go online.

Fig. 5 C, is inside of the invaginated tubules. This observation shows that the I-BAR domains are enriched in the tubules compared to rather flat GUV membranes, consistent with the previous study (12). Moreover, we observed that the invaginated tubules are localized at the intersections of the membrane indentation (i.e., the inward deformation of the circular cross section of the GUV) (Fig. 5 A, arrows). Besides tubulation, to our surprise, we observed that the I-BAR domain deforms GUV membranes into bulges where the I-BAR domain accumulates around their bases, which appear as local indentations. The bulges vary in size from a few microns in Fig. 5 B to a few hundred nanometers in Fig. 5 D. Many bulges with accumulated I-BAR domains produce a "flower-like" structure, as shown in Fig. 5, B and D. This behavior appears to be quite similar to that predicted by the simulations shown in Fig. 4 B.

DISCUSSION

In this article, we utilized a combined multiscale simulation and experimental approach to understand I-BAR domain
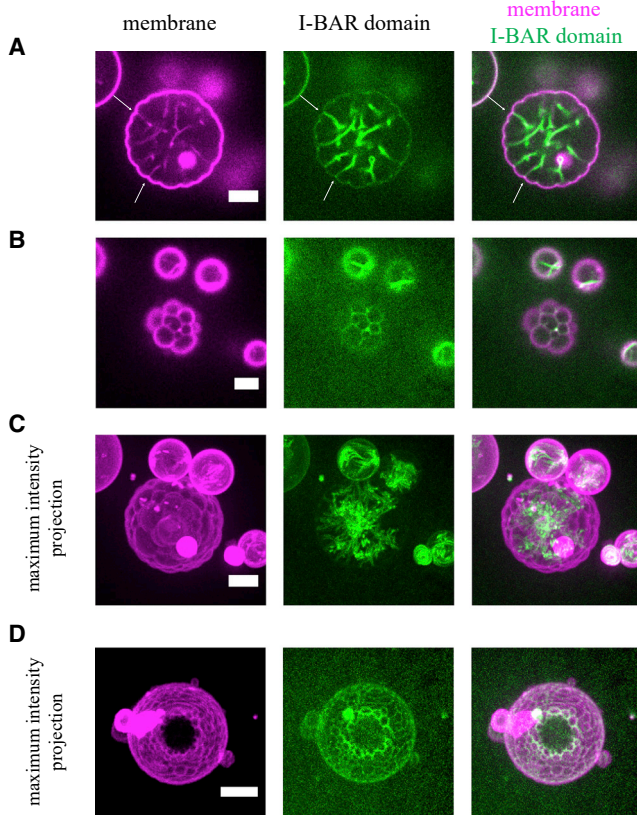
FIGURE 5 IRSp53 I-BAR domain induced flower-like GUV membranes. (*A* and *B*) Shown are the representative confocal images of a GUV in the presence of IRSp53 I-BAR domain. Confocal images were taken at the equator of the GUV (*A*) and at the top of the GUV (*B*). Arrows in (*A*) indicate some membrane indentations. (*C*) Maximal intensity projection of the same GUV is shown in (*A*) and (*B*). (*D*) Maximal intensity projection of a flower-like GUV in the presence of IRSp53 I-BAR domain is shown. Protein concentrations are as follows: (*A*–*C*) 0.02 μM (70% unlabeled and 30% AX488-labeled I-BAR domain) and (*D*) 0.1 μM AX488-labeled I-BAR domain. Scale bars, 5 μm. To see this figure in color, go online.

organization at low surface coverage on lipid bilayers in vitro. We showed that I-BAR domains at a low surface coverage prefer to organize into axial aggregates inside membrane tubules and organize around the periphery of membrane bulges on simulated vesicles and experimentally imaged GUVs. Using separate and complementary CG and mesoscopic approaches to capture protein shape and membrane curvature, we find evidence for robust levels of I-BAR organization. We find transient linear strings at low protein density on the membrane surface through a purely membrane-mediated attraction. As each I-BAR domain deforms the membrane locally, multiple I-BAR domains are attracted to generate long troughs on the surface of GUVs, inside of tubules, and on 200-nm diameter vesicles. We modeled a variety of geometries to approximate the fundamental conditions and curvatures found in experiments, especially in GUVs, as shown in Fig. 5. When the membrane has inherent curvature (i.e., is not locally flat), both

the CG and MesM-P I-BAR domain models couple to the curvature of the membrane and preferentially orient to minimally deform the membrane. The minimal perturbation results in axial aggregates in tubules and rings around membrane bulges.

I-BAR domains form axial aggregates at low coverage

The aggregation behavior shown in the vesicle and tubule simulations suggest a mechanism by which tubules are initiated. Areas where multiple I-BAR aggregates contact are the regions of highest curvature in the flat membrane sheet simulations shown in Fig. 2 *B* and in the 200-nm vesicle simulations shown in Fig. 4 *A*. In the simulation models presented here, the effective attraction between the ends of I-BAR domains is membrane mediated such that the coupling of curvature minimizes the system free energy. In a more realistic bilayer, such as the in vitro assays presented here, the positively charged ends of I-BAR domains could also be electrostatically attracted by the clustering of negatively charged lipids (e.g., phosphatidylinositol 4,5-biphosphate). After the initial nucleation of the tubule, it is unclear how the growth is driven. Although the models here show that the axial aggregate is the preferred orientation, further studies (e.g., simulations of nascent tubules or experiments investigating the orientation of the I-BAR domains at a moderate density inside tubules) will be required in the future to fully elucidate the tubulation mechanism.

The axial aggregates of I-BAR domains inside tubular membranes seen in our simulations are unexpected. We find that I-BAR domains organize such that the grooves in the membrane formed by I-BAR domains produce minimal deformations of the membrane, resulting in long axial troughs that are parallel to the tubule axis. At the surface densities simulated here, the differences between tubule radii most notably affects the orientation of the individual I-BAR domains and the propensity for axial aggregates to form. Our results suggest that the preferred curvature of I-BAR domains may arise from the balance between energetic preference of axial aggregates, which minimally perturb the membrane, and entropic penalty due to reduced rotational freedom inside of the tubule.

As protein surface density increases, we would expect that the axial aggregates would instead form the proposed perpendicular aggregates (14,15), similar to those formed by other members of the BAR family (44–47). At high surface densities, the properties of a single I-BAR domain would also be different because of the presence of the neighboring I-BAR domains, and the resultant local deformation caused by each I-BAR domain could change from the deformations generated by the current model. Given the computational cost of resolving many I-BAR domains at a finer resolution, the current model parameterization also does not take into account direct interactions between

neighboring I-BAR domains (except excluded volume), and therefore, high density conditions are outside of the scope of this model. We also note that axial aggregates are in contrast to previous computational studies of I-BAR domains (14,15) that show perpendicular aggregates inside of membrane tubules, but these previous studies used models unlike the models presented here. Among the several differences including membrane representation and protein-membrane interactions, the CG I-BAR model used in this work reproduces the properties of a single, isolated, and atomically resolved I-BAR domain, which flattens when bound to the membrane and is outside the curvature ranges previously studied. Our model shows a new phenomenology because our multiscale approach considers I-BAR domain properties outside the scope of the previous models to date.

I-BAR domains aggregate around bulges on vesicular membrane at low coverage

We experimentally revealed low curvature bulges that are surrounded by I-BAR domains at their bases, shown in Fig. 5, *B* and *D*. Low surface coverage membrane remodeling of this kind has not been shown before to our knowledge. In addition, in the simulations, we observed consistent aggregation behavior of I-BAR domains on the surface of small vesicles and around the base of preformed membrane bulges in planar membranes. The bulges due to I-BAR domain aggregation here bear a striking resemblance to the deformation modeled by endophilin Bin/amphiphysin/Rvs domains (42) and spherical nanoparticles (48,49). This common phenomenology suggests that the formation of membrane bulges are not specific to I-BAR domains but are the result of emergent phenomenon due to linear aggregation. Furthermore, Fig. 4 *A* shows significant deformation of the surface of small vesicles similar to the experimental images shown in Fig. 5 *B*, although on a smaller length scale. As these simulated vesicles are 100 times smaller than the experimentally relevant vesicles shown in Fig. 5, we also employed the MesM-P-based approach using a spherical guiding potential to form a "dome" structure with Gaussian curvature on a planar membrane. When the membrane is perturbed into a ∼325-nm diameter dome, which is much closer to the size of the membrane bulges shown in Fig. 5 *D*, I-BAR domains aggregate around the edge of the surface, forming a tip-to-tip ring, as shown in Fig. 4 *B*. This result is striking because it resembles the CG result at a shorter length scale, in which Gaussian curvature was generated on a small vesicle as well as the experimental result that shows significant aggregation around the large indentations created by the membrane-bound I-BAR domains.

The phenomenological similarities between I-BAR domain aggregation around the small bulge on the CG vesicle, tip-to-tip ring around the preformed dome on the MesM-P sheet, and the aggregation at the periphery of flower-like membrane structures in experimental images suggest a common driving force acting at different length scales. In the case of the simulations, I-BAR domains bind to the membrane and generate local deformation that leads to aggregation. Given the similar phenomenology, we suggest that the bulges seen in this experiment are a minimally perturbative conformation due to I-BAR domain aggregation.

CONCLUSION

Our multiscale modeling approach captures the local behavior of an isolated, membrane-bound I-BAR domain of IRSp53 and is used to model I-BAR domains on lipid bilayers of various geometries and scales to micron-size systems. We demonstrate that lipid bilayer geometry is an important factor in I-BAR domain aggregation. At low surface coverage, we show that I-BAR domains generate local troughs, leading to transient tip-to-tip aggregates on flat surfaces, and the preference for trough formation leads to string aggregates along the long axis of tubules and a ring of I-BAR domains at the base of membrane bulges on the surface of vesicles. The aggregation behavior demonstrated in the CG and MesM-P simulations provides a mechanism for the intriguing low curvature membrane bulges that we observe experimentally.

SUPPORTING MATERIAL

AUTHOR CONTRIBUTIONS

ACKNOWLEDGMENTS

REFERENCES

1. McMahon, H. T., and J. L. Gallop. 2005. Membrane curvature and mechanisms of dynamic cell membrane remodelling. *Nature.* 438:590–596.

2. Frost, A., V. M. Unger, and P. De Camilli. 2009. The BAR domain superfamily: membrane-molding macromolecules. *Cell.* 137:191–196.

3. Simunovic, M., G. A. Voth, …, P. Bassereau. 2015. When physics takes over: BAR proteins and membrane curvature. *Trends Cell Biol.* 25:780–792.

4. Millard, T. H., G. Bompard, …, K. Fütterer. 2005. Structural basis of filopodia formation induced by the IRSp53/MIM homology domain of human IRSp53. *EMBO J.* 24:240–250.

5. Mattila, P. K., and P. Lappalainen. 2008. Filopodia: molecular architecture and cellular functions. *Nat. Rev. Mol. Cell Biol.* 9:446–454.

6. Ahmed, S., W. I. Goh, and W. Bu. 2010. I-BAR domains, IRSp53 and filopodium formation. *Semin. Cell Dev. Biol.* 21:350–356.

7. Linkner, J., G. Witte, …, J. Faix. 2014. The inverse BAR domain protein IBARa drives membrane remodeling to control osmoregulation, phagocytosis and cytokinesis. *J. Cell Sci.* 127:1279–1292.

8. Zimmerberg, J., and M. M. Kozlov. 2006. How proteins produce cellular membrane curvature. *Nat. Rev. Mol. Cell Biol.* 7:9–19.

9. Saarikangas, J., H. Zhao, …, P. Lappalainen. 2009. Molecular mechanisms of membrane deformation by I-BAR domain proteins. *Curr. Biol.* 19:95–107.

10. Mattila, P. K., A. Pykäläinen, …, P. Lappalainen. 2007. Missing-in-metastasis and IRSp53 deform PI(4,5)P2-rich membranes by an inverse BAR domain-like mechanism. *J. Cell Biol.* 176:953–964.

11. Baumgart, T., B. R. Capraro, …, S. L. Das. 2011. Thermodynamics and mechanics of membrane curvature generation and sensing by proteins and lipids. *Annu. Rev. Phys. Chem.* 62:483–506.

12. Prévost, C., H. Zhao, …, P. Bassereau. 2015. IRSp53 senses negative membrane curvature and phase separates along membrane tubules. *Nat. Commun.* 6:8529.

13. Ramakrishnan, N., P. B. Sunil Kumar, and J. H. Ipsen. 2013. Membrane-mediated aggregation of curvature-inducing nematogens and membrane tubulation. *Biophys. J.* 104:1018–1028.

14. Mesarec, L., W. Góźdź, …, A. Iglič. 2016. Closed membrane shapes with attached BAR domains subject to external force of actin filaments. *Colloids Surf. B Biointerfaces.* 141:132–140.

15. Noguchi, H. 2016. Membrane tubule formation by banana-shaped proteins with or without transient network structure. *Sci. Rep.* 6:20935.

16. Noguchi, H., and J. B. Fournier. 2017. Membrane structure formation induced by two types of banana-shaped proteins. *Soft Matter.* 13:4099–4111.

17. Takemura, K., K. Hanawa-Suetsugu, …, A. Kitao. 2017. Salt bridge formation between the I-BAR domain and lipids increases lipid density and membrane curvature. *Sci. Rep.* 7:6808.

18. Saunders, M. G., and G. A. Voth. 2013. Coarse-graining methods for computational biology. *Annu. Rev. Biophys.* 42:73–93.

19. Davtyan, A., M. Simunovic, and G. A. Voth. 2017. The mesoscopic membrane with proteins (MesM-P) model. *J. Chem. Phys.* 147:044101.

20. Srivastava, A., and G. A. Voth. 2013. A hybrid approach for highly coarse-grained lipid bilayer models. *J. Chem. Theory Comput.* 9:750–765.

21. Plimpton, S. 1995. Fast parallel algorithms for short-range molecular dynamics. *J. Comput. Phys.* 117:1–19.

22. de Groot, J. C., K. Schlüter, …, T. E. Stradal. 2011. Structural basis for complex formation between human IRSp53 and the translocated intimin receptor Tir of enterohemorrhagic E. coli. *Structure.* 19:1294–1306.

23. Best, R. B., X. Zhu, …, A. D. Mackerell, Jr. 2012. Optimization of the additive CHARMM all-atom protein force field targeting improved sampling of the backbone φ, ψ and side-chain χ(1) and χ(2) dihedral angles. *J. Chem. Theory Comput.* 8:3257–3273.

24. Klauda, J. B., R. M. Venable, …, R. W. Pastor. 2010. Update of the CHARMM all-atom additive force field for lipids: validation on six lipid types. *J. Phys. Chem. B.* 114:7830–7843.

25. MacKerell, A. D., D. Bashford, …, M. Karplus. 1998. All-atom empirical potential for molecular modeling and dynamics studies of proteins. *J. Phys. Chem. B.* 102:3586–3616.

26. Jo, S., T. Kim, and W. Im. 2007. Automated builder and database of protein/membrane complexes for molecular dynamics simulations. *PLoS One.* 2:e880.

27. Jo, S., T. Kim, …, W. Im. 2008. CHARMM-GUI: a web-based graphical user interface for CHARMM. *J. Comput. Chem.* 29:1859–1865.

28. Jo, S., J. B. Lim, …, W. Im. 2009. CHARMM-GUI Membrane Builder for mixed bilayers and its application to yeast membranes. *Biophys. J.* 97:50–58.

29. Lee, J., X. Cheng, …, W. Im. 2016. CHARMM-GUI input generator for NAMD, GROMACS, AMBER, OpenMM, and CHARMM/OpenMM simulations using the CHARMM36 additive force field. *J. Chem. Theory Comput.* 12:405–413.

30. Wu, E. L., X. Cheng, …, W. Im. 2014. CHARMM-GUI Membrane Builder toward realistic biological membrane simulations. *J. Comput. Chem.* 35:1997–2004.

31. Abraham, M. J., T. Murtola, …, E. Lindahl. 2015. GROMACS: high performance molecular simulations through multi-level parallelism from laptops to supercomputers. *SoftwareX.* 1–2:19–25.

32. Zhang, Z., L. Lu, …, G. A. Voth. 2008. A systematic methodology for defining coarse-grained sites in large biomolecules. *Biophys. J.* 95:5073–5083.

33. Lyman, E., J. Pfaendtner, and G. A. Voth. 2008. Systematic multiscale parameterization of heterogeneous elastic network models of proteins. *Biophys. J.* 95:4183–4192.

34. Allen, M. P., and D. J. Tildesley. 1989. Computer Simulation of Liquids. Clarendon Press, Oxford, UK.

35. Helfrich, W. 1973. Elastic properties of lipid bilayers: theory and possible experiments. *Z. Naturforsch. C.* 28:693–703.

36. Yu, S., K. Cho, …, H. B. Oh. 2006. Identification of phospholipid molecular species in porcine brain extracts using high mass accuracy of 4.7 Tesla Fourier transform ion cyclotron resonance mass spectrometry. *Bull. Korean Chem. Soc.* 27:793–796.

37. van der Wel, C., A. Vahid, …, D. J. Kraft. 2016. Lipid membrane-mediated attraction between curvature inducing objects. *Sci. Rep.* 6:32825.

38. Goullian, M., R. Bruinsma, and P. Pincus. 1993. Long-range forces in heterogeneous fluid membranes. *Europhys. Lett.* 22:145–150.

39. Aranda-Espinoza, H., A. Berman, …, S. Safran. 1996. Interaction between inclusions embedded in membranes. *Biophys. J.* 71:648–656.

40. Simunovic, M., A. Srivastava, and G. A. Voth. 2013. Linear aggregation of proteins on the membrane as a prelude to membrane remodeling. *Proc. Natl. Acad. Sci. USA.* 110:20396–20401.

41. Simunovic, M., and G. A. Voth. 2015. Membrane tension controls the assembly of curvature-generating proteins. *Nat. Commun.* 6:7219.

42. Simunovic, M., A. Šarić, …, G. A. Voth. 2017. Long-range organization of membrane-curving proteins. *ACS Cent. Sci.* 3:1246–1253.

43. Barooji, Y. F., A. Rørvig-Lund, …, P. M. Bendix. 2016. Dynamics of membrane nanotubes coated with I-BAR. *Sci. Rep.* 6:30054.

Jarin et al.

44. Mim, C., H. Cui, ..., V. M. Unger. 2012. Structural basis of membrane bending by the N-BAR protein endophilin. *Cell.* 149:137–145.

45. Frost, A., R. Perera, ..., V. M. Unger. 2008. Structural basis of membrane invagination by F-BAR domains. *Cell.* 132:807–817.

46. Daum, B., A. Auerswald, ..., A. Meister. 2016. Supramolecular organization of the human N-BAR domain in shaping the sarcolemma membrane. *J. Struct. Biol.* 194:375–382.

47. Cui, H., C. Mim, ..., G. A. Voth. 2013. Understanding the role of amphipathic helices in N-BAR domain driven membrane remodeling. *Biophys. J.* 104:404–411.

48. Šarić, A., and A. Cacciuto. 2012. Fluid membranes can drive linear aggregation of adsorbed spherical nanoparticles. *Phys. Rev. Lett.* 108:118101.

49. Šarić, A., and A. Cacciuto. 2013. Self-assembly of nanoparticles adsorbed on fluid and elastic membranes. *Soft Matter.* 9:6677.

Supplemental Information

Unusual Organization of I-BAR Proteins on Tubular and Vesicular Membranes

Zack Jarin, Feng-Ching Tsai, Aram Davtyan, Alexander J. Pak, Patricia Bassereau, and Gregory A. Voth

Unusual Organization of I-BAR Proteins on Tubular and Vesicular Membranes

Z Jarin, F-C Tsai, A Davtyan, A J Pak, P Bassereau, G A Voth

CG Model Details

The coarse-grained (CG) models used in this study were systematically parameterized from reference all-atom simulations. We first describe the atomistic simulations used, then the procedure to train and simulate the coarse-grained models.

All-atom simulation details

All-atom simulations of a single I-BAR domain of IRSp53 interacting with a fully solvated, periodic lipid bilayer were run using GROMACS (version 5.0) (1). Initially, a lipid bilayer composed of 75% 1,2-dioleoyl-sn-glycero-3-phosphocholine (DOPC), 20% 1,2-dioleoyl-sn-glycero-3-phosphoserine (DOPS), and 5% Phosphatidylinositol-4,5-diphosphate (PI(4,5)P$_2$) was generated using the CHARMM-GUI and equilibrated using the CHARMM-GUI scheme of sequentially restrained simulations (2-6). Next, the I-BAR domain of IRSp53 (PDB: 2YKT(7)) was added to the membrane, and solvated with 150 mM NaCl using GROMACS tools (1). Production simulations were run at 298 K at 1 atm using a Nose-Hoover thermostat and the Parrinello-Rahman barostat implemented with corresponding 1 ps and 5.0 ps coupling constants in GROMACS (1, 8, 9). The CHARMM36 force-field was used in all simulations as well (10-12).

CG model details

A coarse-grained map of I-BAR domain of IRSp53 was created using Essential Dynamics Coarse-graining (ED-CG) using 24 beads per monomer (13). This number of beads was chosen to reproduced to maintain a similar resolution between the protein and lipid model, which has been thoroughly described ref (14). The ED-CG protocol generates a mapping dividing the protein along its primary sequence by minimizing the residual (shown in Eq. 1) describing the fluctuations between beads.

$$\chi^2 = \frac{1}{3N}\sum_{I=1}^{N}\frac{1}{n_t}\sum_{t=1}^{n_t}\left(\sum_{i\in I}\sum_{j\geq i\in I}\left|\Delta r_i^{ED}(t) - \Delta r_j^{ED}(t)\right|^2\right) \tag{1}$$

where N is the number of CG sites, n_t is the number of configuration, and Δr_i^{ED} is the displacement from equilibrium of the ith CG site at configuration t. The protocol used here first maps each residue to the carbon-alpha atom of the residue backbone, then maps multiple carbon-alpha atoms to a single bead resulting in approximately 10 residues per bead. For example, the boundaries for the first bead are the first residue and the fourth residue i.e. the first three residues' carbon alphas map to the first bead. As a result of a steepest descent and simulated annealing minimization scheme, the residue boundaries between beads are as follows, 1st, 4th, 8th, 20th 35th, 48th, 63rd, 77th, 90th, 105th, 114th, 127th, 138th, 147th, 152nd, 156th, 160th, 167th, 177th, 190th, 202nd, 216th, 226th, and 236th. The spacing is not regular as ED-CG optimizes these boundaries to maximally capture the atomistic fluctuations in the protein. The intraprotein interactions are parameterized using a hetero-elastic network model parameterized using the all-atom simulations (15). Parameters, k_{ij} and b_{ij} shown in Eq. 2, between each pair of CG protein beads are determined to reproduce the fluctuations

of the CG beads in the mapped all-atom trajectory. In Table 1, the intraprotein elastic network parameters are shown.

$$U_b(r_{ij}) = k_{ij}(r_{ij} - b_{ij})^2 \tag{2}$$

The interprotein and protein-lipid (nonbonded) interactions use a shifted-force 10-6 Lennard Jones potential defined below (16). Both interprotein and protein-lipid interactions used a sigma value of 1.5 nm, which was the most probable distance between mapped protein beads to the mapped lipid head groups. The nonbonded interaction cutoff was assumed to be 2σ. The epsilon values of the protein-lipid interactions were investigated as described in the main document. The interprotein interactions were the repulsive portion of the protein-lipid interaction.

$$U_{NB} = U_{LJ}(r_{ij}) - U_{LJ}(r_c) - (r - r_c) F_{LJ}(r_c), \qquad r < r_C \tag{3}$$

$$U_{LJ}(r_{ij}) = 4\epsilon \left[\left(\frac{\sigma}{r_{ij}}\right)^{10} - \left(\frac{\sigma}{r_{ij}}\right)^6 \right] \quad \text{and} \quad F_{LJ}(r_{ij}) = -U'_{LJ}(r_{ij}) \tag{4}$$

The initial configurations for each system were created by placing lipids on equally spaced points in the desired geometry (e.g., cylinder) and equilibrating under zero membrane tension when applicable. Proteins were subsequently added to the equilibrated lipid bilayer system. CG simulations were run using the LAMMPS MD engine and the Langevin thermostat with temperature dampening parameter of 5000fs and Parrinello-Rahman barostat with pressure dampening parameter of 50,000fs (8, 17, 18). The timescale of the production simulations was at least 30 million steps with a coarse-grained timestep of 5 fs, but varied based on the geometry and the time required to converge order parameters statistics described in the main text.

MesM-P Model Details

The MesM-P model leverages successes of the original MesM-P model with three major changes: no solvent, softer 10-2 Lennard-Jones potential, and shorter discretization length (19). We set the discretization of the membrane mesh to approximately 3 nm, based on the dimensions of the I-BAR domain of IRSp53 (7). Next, we parametrize the I-BAR domain model as a linear chain of MesM-P particles with varied radii. The protein-membrane interactions use a shifted-force 4-2 Lennard Jones potential similar to that shown above. In the protein-membrane interactions, we use values of sigma equal to 2.67, 2.90, and 3.12 nm and corresponding values of epsilon equal to 1.0, 1.25, and 1.5 kcal/mol, which capture the shape and aggregation behavior of the I-BAR domain as shown in the main text. The protein-protein interactions were the repulsive portion of the protein membrane interaction with the same varied sigma values to maintain the shape of the I-BAR domains.

The initial configurations for each system were made by placing membrane beads on a hexagonal lattice in the desired geometry and equilibrating under zero tension using the Langevin thermostat with temperature dampening parameter of 5000fs and Berendsen barostat with pressure dampening parameter of 50000fs. All systems ran for 5 million timesteps to converge order parameter statistics described in main text. The guiding potential used to generate the membrane bulge as described in the main text was a 325 nm spherical guiding potential slowly moved toward the membrane under zero tension. The spherical surface had a potential form of a 9-3 Lennard Jones similar to the potential shown in Equation 4 with a value of 1 kcal/mol.

CG Protein-Protein Interactions

Thus far, we have assumed that the protein-protein interactions are purely repulsive, i.e., direct attraction between protein beads is not included. In reality, there would be some degree of protein-protein interaction. I-BAR domains are significantly charged proteins, which directly affects the membrane binding behavior. If each CG bead is assigned the mapped net charge, i.e., a simple charge mapping, we find a positively charge protein surface near the membrane and a positive high charge density near the ends of the I-BAR domains, as shown in Fig. S1A. The protein shown similarly to Figure 1A of the main text, and the membrane would lie directly below the I-BAR domain in this view. We note a positively charge protein surface near the membrane and the high charge density near the ends of the I-BAR domain. Additionally, there is a net +3 charge on a CG single bead, which in an atomistic resolution would be delocalized over several residues. In the absence of explicit solvent, we model screened electrostatic interactions between two I-BAR domains with a Yukawa potential with the unknown screening length, κ, shown in Equation 5.

$$V_{Yukawa}(r) = -\frac{q_1 q_2}{4\pi\epsilon_0}\frac{e^{-\kappa r}}{r} \tag{5}$$

In the bulk, we could approximate the experimental screening length corresponding to 20 mM Tris pH 7.5, 60 mM NaCl and 100 mM sucrose buffer, but published studies[20, 21] have shown the effective ion concentration near the membrane is higher than in the bulk. We ran simulations using the possible screening lengths from near bulk ion concentration ($\kappa = 0.15$ Å^{-1}) to ~10x increase in effective ion concentration ($\kappa = 0.45$ Å^{-1}). We characterize these aggregates using the same order parameter analysis described in the main text and shown in panel B of Fig S1.

A

B

C
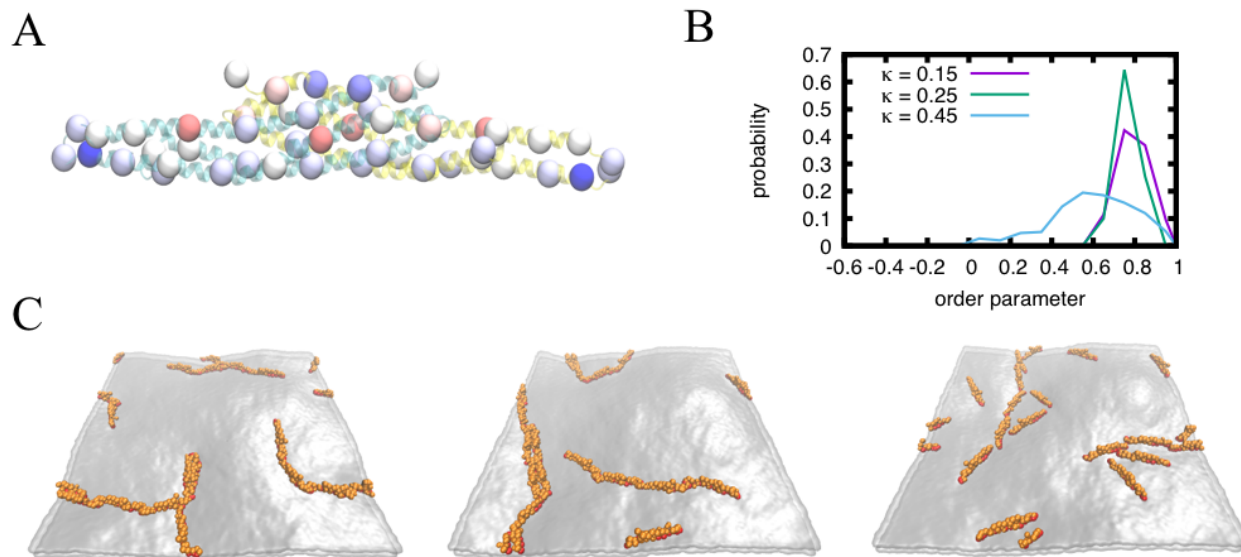
Figure S1. Charge distribution on CG model and snapshots of flat sheet configurations with screened electrostatic interactions. A) Side view of an overlay of the secondary structure of each monomer (cyan and yellow) and CG I-BAR domain colored by charge (+3 charge [blue], -2 [red]) B) probability distribution of inter-protein order parameter for varied screening lengths. C) snapshot of 10% coverage of a 100nm by 100nm flat at varied screening length: 0.15 Å^{-1}, 0.25 Å^{-1}, and 0.45 Å^{-1} from left to right.

As seen in panels B and C of Fig. S1, at low effective ion concentration ($\kappa = 0.15$ Å^{-1}), the I-BAR domains begin to form bundled linear aggregates. This behavior is due to an overestimation of the protein-protein interactions because of the low effective salt concentration and the localization of charge on a single CG bead. At 3x bulk ion concentration ($\kappa = 0.25$ Å^{-1}), I-BAR domains again form more unbundled linear aggregates with some additional side-to-side character, as additional I-BAR domains move to align opposite charges on the I-BAR domains. This behavior is expected at more reasonable bulk ion concentration. Finally, at 10x bulk ion concentration ($\kappa = 0.45$ Å^{-1}), we find mostly linear aggregates again. Thus, when we model the electrostatic interactions between I-BAR domains in this way, we find that aggregation behavior qualitatively agrees with that from purely repulsive excluded volume protein interactions, which is to say that linear tip-to-tip aggregation is dominant and that this behavior is the result of an indirect membrane-mediated force.

Table 1: Heterogenous Elastic Network Model of CG I-BAR Domain. Indices 1-24 and 25-48 are each monomers of the I-BAR dimer.

Bond index	I-BAR site i	I-BAR site j	k_{ij} (kcal/mol/nm)	b_i (nm)
1	1	2	0.157	0.72067
2	1	3	0.051	1.67476
3	1	4	0.035	3.46783
4	1	5	0.025	5.47033
5	1	9	0.022	5.92131
6	1	10	0.026	4.38529
7	1	11	0.037	2.76665
8	1	12	0.932	1.26606
9	1	13	0.038	1.19113
10	1	14	0.006	1.59165
11	1	15	0.004	2.19398
12	1	16	0.006	1.72454
13	1	17	0.008	1.6926
14	1	18	0.726	1.23483
15	1	19	0.849	1.95313
16	1	20	0.042	3.59278
17	1	21	0.031	5.52169
18	1	30	0.024	5.07338
19	1	31	0.034	3.65461
20	1	32	0.026	5.154
21	1	47	0.01	4.80283
22	1	48	0.02	3.94519
23	2	3	5.544	1.28621
24	2	4	0.14	3.19579
25	2	5	0.151	5.18833
26	2	9	0.103	5.62437
27	2	10	0.187	4.18755
28	2	11	1.383	2.70757
29	2	12	1.53	1.46187
30	2	13	0.026	1.73096
31	2	14	0.007	2.0144
32	2	15	0.006	2.49756
33	2	16	0.007	1.80779
34	2	17	0.008	1.81401
35	2	18	0.112	1.25627

36	2	19	7.879	1.64888
37	2	20	0.278	3.23694
38	2	21	0.17	5.14485
39	2	30	0.078	4.68839
40	2	31	0.109	3.16253
41	2	32	0.071	4.68385
42	2	46	0.082	5.60502
43	2	47	0.034	4.34826
44	2	48	0.014	3.53817
45	3	4	0.904	1.96242
46	3	5	0.805	3.93522
47	3	9	0.332	4.34665
48	3	10	0.447	2.93438
49	3	11	22.021	1.63069
50	3	12	11.871	1.33705
51	3	13	0.623	2.63767
52	3	14	0.027	3.17265
53	3	15	0.008	3.66688
54	3	16	0.012	3.04643
55	3	17	0.042	2.9471
56	3	18	7.804	2.01619
57	3	19	45.888	0.93958
58	3	20	30.126	1.9864
59	3	21	0.566	3.89337
60	3	22	4.026	5.69693
61	3	29	10.535	5.58022
62	3	30	0.182	3.47394
63	3	31	0.142	2.002
64	3	32	0.133	3.49711
65	3	33	0.312	5.37109
66	3	45	0.518	5.86174
67	3	46	0.138	4.41816
68	3	47	0.049	3.20181
69	3	48	0.215	2.55673
70	4	5	105.148	2.01061
71	4	6	15.51	4.16504
72	4	7	1.539	5.93097
73	4	8	0.333	4.57014
74	4	9	1.063	2.63051
75	4	10	0.765	1.30486
76	4	11	30.53	1.37257
77	4	12	3.678	2.77714
78	4	13	0.084	4.3937
79	4	14	0.017	4.97111
80	4	15	0.004	5.41424
81	4	16	0.008	4.92109
82	4	17	0.051	4.88414
83	4	18	0.277	3.89841
84	4	19	0.396	2.37234
85	4	20	27.842	1.21186
86	4	21	9.762	2.45227
87	4	22	10.827	4.16281
88	4	23	0.466	5.38916
89	4	28	0.619	5.66204
90	4	29	3.837	3.68981
91	4	30	0.353	1.73921

92	4	31	24.824	1.39215
93	4	32	0.664	2.15746
94	4	33	0.747	3.67121
95	4	34	0.29	5.08677
96	4	44	0.552	5.9
97	4	45	0.802	4.19729
98	4	46	0.472	3.13055
99	4	47	0.202	2.41756
100	4	48	0.005	2.54493
101	5	6	45.734	2.16872
102	5	7	19.259	3.97299
103	5	8	0.304	2.71107
104	5	9	56.299	1.15941
105	5	10	0.313	1.49844
106	5	11	0.191	3.03832
107	5	12	0.251	4.68577
108	5	18	0.674	5.82389
109	5	19	0.567	4.18314
110	5	20	1.119	2.38847
111	5	21	14.294	1.63264
112	5	22	14.076	2.64924
113	5	23	1.869	3.65635
114	5	24	0.724	4.8976
115	5	27	11.57	5.5464
116	5	28	2.268	3.68196
117	5	29	28.581	1.77545
118	5	30	75.667	1.02725
119	5	31	5.607	2.54644
120	5	32	3.063	1.77781
121	5	33	17.757	2.07866
122	5	34	0.802	3.25687
123	5	35	0.371	4.77998
124	5	43	13.979	5.84257
125	5	44	5.312	3.99099
126	5	45	0.675	2.51109
127	5	46	3.462	2.2726
128	5	47	6.301	2.6014
129	5	48	0.004	3.47228
130	6	7	42.079	1.84228
131	6	8	30.511	1.01613
132	6	9	3.442	1.94137
133	6	10	0.913	3.40658
134	6	11	5.248	5.09948
135	6	20	1.263	4.29271
136	6	21	7.913	2.6483
137	6	22	9.276	1.8981
138	6	23	8.22	2.08001
139	6	24	0.509	2.97419
140	6	25	0.001	4.24468
141	6	26	0.007	3.96905
142	6	27	0.157	3.42931
143	6	28	0.305	1.72271
144	6	29	69.728	1.04588
145	6	30	2.679	2.78135
146	6	31	0.5	4.42078
147	6	32	0.268	3.11349

148	6	33	17.334	1.76375
149	6	34	0.655	1.83121
150	6	35	0.233	2.9947
151	6	36	0.168	4.41572
152	6	37	0.117	5.81217
153	6	42	0.242	5.42998
154	6	43	0.224	3.78628
155	6	44	3.3	2.04681
156	6	45	0.555	1.52521
157	6	46	0.296	2.793
158	6	47	0.193	3.90065
159	6	48	0.006	5.04118
160	7	8	0.451	1.50666
161	7	9	12.091	3.51955
162	7	10	0.606	5.13554
163	7	20	0.349	5.89988
164	7	21	0.302	4.04572
165	7	22	0.163	2.50095
166	7	23	3.966	1.55201
167	7	24	0.067	1.45564
168	7	25	0.001	2.55337
169	7	26	0.006	2.20505
170	7	27	0.195	1.91515
171	7	28	22.335	1.40273
172	7	29	0.876	2.59073
173	7	30	0.476	4.44408
174	7	31	0.536	5.98571
175	7	32	0.665	4.54154
176	7	33	0.186	2.89333
177	7	34	1.065	2.11225
178	7	35	2.849	2.26068
179	7	36	0.095	3.11897
180	7	37	0.08	4.35802
181	7	38	0.121	5.2875
182	7	40	0.068	5.66852
183	7	41	0.072	4.96221
184	7	42	0.122	3.805
185	7	43	0.21	2.20225
186	7	44	21.696	1.04014
187	7	45	6.237	2.22118
188	7	46	0.841	3.87393
189	7	47	0.093	5.20378
190	8	9	68.82	2.07031
191	8	10	5.059	3.73619
192	8	11	0.114	5.4378
193	8	20	0.198	4.43006
194	8	21	0.216	2.55541
195	8	22	0.265	1.18895
196	8	23	20.028	1.39495
197	8	24	0.953	2.47085
198	8	25	0.001	3.9512
199	8	26	0.005	3.66932
200	8	27	0.099	3.3883
201	8	28	0.408	2.13006
202	8	29	0.168	1.84705
203	8	30	0.105	3.1741

204	8	31	0.302	4.57779
205	8	32	0.327	3.19577
206	8	33	0.055	2.02378
207	8	34	0.812	2.25619
208	8	35	0.374	3.26643
209	8	36	0.09	4.5016
210	8	37	0.07	5.82844
211	8	42	0.089	5.27441
212	8	43	0.118	3.61619
213	8	44	2.04	1.89881
214	8	45	10.563	1.28128
215	8	46	1.386	2.51662
216	8	47	0.176	3.73432
217	8	48	0.01	4.93198
218	9	10	36.195	1.6856
219	9	11	0.109	3.37636
220	9	12	0.096	5.01007
221	9	19	0.248	4.35228
222	9	20	0.315	2.46801
223	9	21	0.748	0.96599
224	9	22	8.537	1.84659
225	9	23	0.573	3.13593
226	9	24	1.806	4.45707
227	9	25	0.068	5.93647
228	9	26	0.364	5.69178
229	9	27	0.22	5.30425
230	9	28	0.256	3.65102
231	9	29	14.42	2.08446
232	9	30	12.938	1.74039
233	9	31	0.764	2.8325
234	9	32	1.185	1.8969
235	9	33	12.465	2.23946
236	9	34	0.408	3.41697
237	9	35	0.249	4.84781
238	9	43	0.34	5.5861
239	9	44	3.177	3.74528
240	9	45	0.387	2.19358
241	9	46	6.083	1.79227
242	9	47	0.134	2.20616
243	9	48	0.003	3.18199
244	10	11	0.251	1.72458
245	10	12	0.277	3.41935
246	10	13	1.559	5.12251
247	10	14	0.054	5.86738
248	10	16	0.012	5.91282
249	10	17	0.164	5.70769
250	10	18	0.317	4.61824
251	10	19	0.339	2.98906
252	10	20	10.039	1.41065
253	10	21	3.641	1.7958
254	10	22	8.252	3.44731
255	10	23	0.504	4.77085
256	10	28	0.151	5.04749
257	10	29	0.693	3.24221
258	10	30	22.923	1.8423
259	10	31	0.842	2.10261

260	10	32	0.736	2.22537
261	10	33	6.956	3.42676
262	10	34	0.215	4.72064
263	10	44	0.318	5.30907
264	10	45	0.381	3.70361
265	10	46	0.325	2.78998
266	10	47	0.507	2.22394
267	10	48	0.002	2.4968
268	11	12	69.499	1.73151
269	11	13	0.18	3.4337
270	11	14	0.039	4.2105
271	11	15	0.006	4.79613
272	11	16	0.012	4.36094
273	11	17	0.135	4.13693
274	11	18	0.29	3.07696
275	11	19	7.645	1.71042
276	11	20	10.197	1.57909
277	11	21	0.212	3.22352
278	11	22	0.91	5.02939
279	11	29	0.571	4.80664
280	11	30	0.19	3.01484
281	11	31	0.245	2.24014
282	11	32	0.217	3.2867
283	11	33	0.753	4.88777
284	11	45	4.726	5.28011
285	11	46	0.147	4.07452
286	11	47	0.038	2.98872
287	11	48	0.005	2.48693
288	12	13	0.265	1.72076
289	12	14	0.544	2.58217
290	12	15	0.013	3.27135
291	12	16	0.033	2.83371
292	12	17	2.473	2.4968
293	12	18	3.344	1.51159
294	12	19	14.367	1.26472
295	12	20	0.606	2.77833
296	12	21	0.195	4.68308
297	12	30	0.199	4.4599
298	12	31	0.097	3.15395
299	12	32	0.113	4.56429
300	12	46	0.091	5.3872
301	12	47	0.028	4.07016
302	12	48	0.023	3.14937
303	13	14	9.034	1.12617
304	13	15	1.427	1.96107
305	13	16	1.952	1.71085
306	13	17	7.928	1.25037
307	13	18	15.485	1.19683
308	13	19	6.401	2.56683
309	13	20	1.042	4.37675
310	13	31	0.081	4.59449
311	13	47	0.043	5.55008
312	13	48	0.015	4.49255
313	14	15	1.114	0.87504
314	14	16	0.114	0.95271
315	14	17	0.08	1.23054

316	14	18	8.478	1.90432
317	14	19	0.084	3.32567
318	14	20	0.033	5.0789
319	14	31	0.016	5.11535
320	14	48	0.008	5.25932
321	15	16	1.418	1.01069
322	15	17	0.024	1.80918
323	15	18	2.682	2.61775
324	15	19	0.014	3.94812
325	15	20	0.006	5.61121
326	15	31	0.005	5.53346
327	15	48	0.004	5.83937
328	16	17	0.092	1.11345
329	16	18	1.396	1.9107
330	16	19	0.011	3.25537
331	16	20	0.007	4.96865
332	16	31	0.006	4.84759
333	16	48	0.003	5.09493
334	17	18	52.358	1.18257
335	17	19	4.726	2.83744
336	17	20	0.148	4.71213
337	17	31	0.056	4.74436
338	17	47	0.037	5.68279
339	17	48	0.009	4.62069
340	18	19	70.074	1.71897
341	18	20	0.962	3.63203
342	18	21	0.364	5.53978
343	18	30	0.213	5.41822
344	18	31	0.207	3.79104
345	18	32	0.162	5.3013
346	18	47	0.034	4.63895
347	18	48	0.008	3.55428
348	19	20	1.053	1.92276
349	19	21	0.446	3.83058
350	19	22	11.778	5.64721
351	19	29	3.495	5.86731
352	19	30	0.299	3.80701
353	19	31	0.341	2.22356
354	19	32	0.191	3.67124
355	19	33	0.377	5.63841
356	19	45	1.294	5.98858
357	19	46	0.155	4.4064
358	19	47	0.038	2.9988
359	19	48	0.007	2.04434
360	20	21	1.457	1.94337
361	20	22	33.379	3.77768
362	20	23	0.52	5.18225
363	20	28	0.443	5.91179
364	20	29	0.795	4.0181
365	20	30	0.694	2.0643
366	20	31	50.611	1.00424
367	20	32	4.91	1.92312
368	20	33	0.544	3.801
369	20	34	0.353	5.36338
370	20	44	0.481	5.9445
371	20	45	1.584	4.09697

372	20	46	0.536	2.62321
373	20	47	0.066	1.43876
374	20	48	0.003	1.39405
375	21	22	69.497	1.84558
376	21	23	18.368	3.29543
377	21	24	0.098	4.73905
378	21	27	0.262	5.87363
379	21	28	0.571	4.27775
380	21	29	0.346	2.6407
381	21	30	0.665	1.6226
382	21	31	2.838	2.18921
383	21	32	37.178	1.26901
384	21	33	0.173	2.36246
385	21	34	0.482	3.83822
386	21	35	0.545	5.35045
387	21	44	0.62	4.15002
388	21	45	27.453	2.32561
389	21	46	37.503	1.09329
390	21	47	0.114	1.28433
391	21	48	0.005	2.46054
392	22	23	22.771	1.54625
393	22	24	0.327	2.98984
394	22	25	0.001	4.81836
395	22	26	0.005	4.53855
396	22	27	0.115	4.35544
397	22	28	0.397	3.13494
398	22	29	7.824	2.31194
399	22	30	0.79	2.79418
400	22	31	0.846	3.84795
401	22	32	3.316	2.46218
402	22	33	0.417	1.92348
403	22	34	0.477	2.85748
404	22	35	0.149	4.0897
405	22	36	0.094	5.38569
406	22	43	0.123	4.40107
407	22	44	0.346	2.6344
408	22	45	40.304	1.13455
409	22	46	14.711	1.51197
410	22	47	0.296	2.80438
411	22	48	0.216	4.08026
412	23	24	0.049	1.50858
413	23	25	0.001	3.60707
414	23	26	0.005	3.27573
415	23	27	0.168	3.10142
416	23	28	1.339	2.32029
417	23	29	11.199	2.49636
418	23	30	0.472	3.79278
419	23	31	0.189	5.10669
420	23	32	0.228	3.59536
421	23	33	0.362	2.1373
422	23	34	0.454	2.12042
423	23	35	0.067	2.90401
424	23	36	0.063	4.02381
425	23	37	0.051	5.35106
426	23	41	0.04	5.80316
427	23	42	0.062	4.62131

428	23	43	0.096	2.96284
429	23	44	0.212	1.35572
430	23	45	0.38	1.24906
431	23	46	1.708	2.76403
432	23	47	0.086	4.23579
433	23	48	0.027	5.55257
434	24	25	0.001	2.41384
435	24	26	0.002	2.01988
436	24	27	0.023	2.01261
437	24	28	0.087	2.27372
438	24	29	0.133	3.44004
439	24	30	0.118	5.11667
440	24	32	0.044	5.02159
441	24	33	0.05	3.31154
442	24	34	0.708	2.49359
443	24	35	0.024	2.31336
444	24	36	0.024	2.85403
445	24	37	0.019	4.02244
446	24	38	0.02	4.90776
447	24	39	0.015	5.65355
448	24	40	0.016	5.21839
449	24	41	0.017	4.3638
450	24	42	0.017	3.20507
451	24	43	0.012	1.64859
452	24	44	0.019	1.19247
453	24	45	0.035	2.60586
454	24	46	0.098	4.24311
455	24	47	0.026	5.71427
456	25	26	0.023	0.82883
457	25	27	0.487	1.66351
458	25	28	0.002	3.14735
459	25	29	0.002	4.90243
460	25	33	0.001	5.20058
461	25	34	0.002	4.02206
462	25	35	0.011	3.08506
463	25	36	0.013	2.41577
464	25	37	0.002	2.75094
465	25	38	0.001	3.52485
466	25	39	0.001	4.19656
467	25	40	0.001	3.62482
468	25	41	0.001	3.02912
469	25	42	0.002	2.18536
470	25	43	0.199	1.81331
471	25	44	0.002	2.8749
472	25	45	0.001	4.57164
473	26	27	1.664	1.16362
474	26	28	0.01	2.81353
475	26	29	0.008	4.61297
476	26	33	0.007	4.88748
477	26	34	0.009	3.67927
478	26	35	0.025	2.71004
479	26	36	0.309	2.11156
480	26	37	0.01	2.66323
481	26	38	0.008	3.51169
482	26	39	0.006	4.2164
483	26	40	0.006	3.66067

484	26	41	0.009	2.98739
485	26	42	0.02	2.00105
486	26	43	0.564	1.3039
487	26	44	0.006	2.48195
488	26	45	0.005	4.2549
489	26	46	0.021	5.9397
490	27	28	0.971	1.95652
491	27	29	1.24	3.91516
492	27	33	0.405	4.29863
493	27	34	11.562	2.86869
494	27	35	12.199	1.68926
495	27	36	12.468	1.37094
496	27	37	5.177	2.46513
497	27	38	2.35	3.39551
498	27	39	0.688	4.21386
499	27	40	0.738	3.85144
500	27	41	3.186	3.21035
501	27	42	10.64	2.08496
502	27	43	41.98	0.917
503	27	44	35.011	1.94764
504	27	45	0.529	3.84402
505	27	46	1.033	5.64131
506	28	29	102.142	2.00602
507	28	30	26.96	4.1551
508	28	31	1.15	5.90133
509	28	32	2.84	4.50849
510	28	33	1.98	2.60714
511	28	34	23.869	1.24932
512	28	35	8.447	1.3753
513	28	36	0.432	2.74411
514	28	37	0.229	4.17757
515	28	38	0.097	5.08376
516	28	39	0.049	5.93774
517	28	40	0.155	5.70091
518	28	41	0.318	5.07467
519	28	42	0.527	3.91359
520	28	43	2.63	2.36973
521	28	44	59.47	1.21298
522	28	45	18.086	2.41257
523	28	46	1.489	4.16748
524	28	47	0.141	5.47126
525	29	30	48.671	2.16797
526	29	31	34.718	3.95677
527	29	32	11.188	2.67107
528	29	33	0.996	1.14339
529	29	34	0.232	1.50795
530	29	35	0.166	3.0102
531	29	36	0.203	4.64989
532	29	42	0.796	5.81704
533	29	43	1.773	4.1717
534	29	44	19.958	2.38201
535	29	45	20.939	1.55098
536	29	46	6.008	2.68271
537	29	47	3.588	3.77384
538	29	48	0.008	4.92769
539	30	31	85.543	1.82484

540	30	32	63.726	0.99779
541	30	33	12.025	1.94261
542	30	34	6.674	3.43993
543	30	35	3.389	5.06669
544	30	44	0.807	4.26651
545	30	45	1.26	2.55704
546	30	46	25.661	1.90322
547	30	47	9.947	2.17974
548	30	48	0.018	3.14438
549	31	32	1.018	1.53642
550	31	33	4.011	3.52897
551	31	34	0.624	5.1627
552	31	44	0.329	5.85704
553	31	45	0.442	3.96656
554	31	46	0.272	2.47624
555	31	47	2.901	1.54966
556	31	48	0.403	1.87535
557	32	33	61.001	2.06571
558	32	34	16.025	3.74049
559	32	35	13.839	5.36457
560	32	44	0.607	4.35289
561	32	45	1.606	2.44643
562	32	46	0.544	1.15229
563	32	47	11.484	1.44203
564	32	48	0.125	2.64685
565	33	34	0.625	1.6918
566	33	35	0.348	3.31317
567	33	36	0.255	4.96018
568	33	43	0.371	4.32106
569	33	44	0.471	2.45144
570	33	45	10.731	0.97636
571	33	46	3.958	1.96215
572	33	47	4.278	3.26989
573	33	48	0.405	4.55638
574	34	35	0.79	1.64685
575	34	36	0.443	3.34686
576	34	37	0.51	4.88467
577	34	38	0.403	5.76317
578	34	41	0.21	5.72765
579	34	42	0.488	4.53735
580	34	43	7.23	2.93556
581	34	44	14.643	1.38172
582	34	45	8.555	1.81806
583	34	46	1.011	3.52568
584	34	47	0.514	4.89162
585	35	36	48.533	1.74049
586	35	37	1.778	3.28327
587	35	38	0.174	4.14304
588	35	39	0.026	4.99755
589	35	40	0.048	4.8754
590	35	41	0.253	4.21123
591	35	42	0.255	3.06996
592	35	43	2.661	1.73749
593	35	44	6.793	1.58676
594	35	45	0.349	3.20926
595	35	46	1.05	5.0327

596	36	37	82.511	1.55138
597	36	38	0.311	2.42869
598	36	39	0.041	3.28898
599	36	40	0.066	3.1487
600	36	41	0.402	2.53341
601	36	42	6.272	1.50949
602	36	43	3.088	1.29266
603	36	44	1.59	2.77502
604	36	45	0.285	4.68144
605	37	38	8.365	0.94399
606	37	39	1.073	1.82176
607	37	40	0.531	1.65835
608	37	41	3.969	1.29772
609	37	42	3.256	1.12448
610	37	43	0.43	2.41174
611	37	44	0.431	4.19524
612	38	39	0.104	0.95919
613	38	40	0.436	1.09773
614	38	41	1.498	1.26418
615	38	42	2.226	1.82715
616	38	43	1.065	3.3145
617	38	44	0.851	5.11477
618	39	40	4.197	0.89083
619	39	41	1.564	1.59492
620	39	42	0.629	2.5102
621	39	43	0.433	4.10042
622	39	44	0.273	5.93457
623	40	41	3.825	1.0315
624	40	42	2.769	2.08683
625	40	43	0.242	3.73676
626	40	44	0.313	5.61278
627	41	42	14.881	1.22155
628	41	43	0.985	2.92954
629	41	44	0.28	4.83764
630	42	43	70.754	1.71484
631	42	44	0.619	3.62667
632	42	45	0.206	5.54581
633	43	44	0.841	1.91735
634	43	45	0.305	3.8395
635	43	46	0.495	5.63309
636	44	45	1.009	1.94795
637	44	46	13.447	3.77456
638	44	47	0.107	5.22822
639	45	46	33.545	1.84665
640	45	47	0.414	3.3115
641	45	48	0.106	4.642
642	46	47	0.382	1.53726
643	46	48	0.117	2.9303
644	47	48	0.036	1.48032

Supplemental References

1.	Abraham, M. J., T. Murtola, R. Schulz, S. Páll, J. C. Smith, B. Hess, and E. Lindahl. 2015. GROMACS: High performance molecular simulations through multi-level parallelism from laptops to supercomputers. *SoftwareX.* 1-2:19-25.
2.	Jo, S., T. Kim, and W. Im. 2007. Automated builder and database of protein/membrane complexes for molecular dynamics simulations. *PLoS One.* 2:e880.
3.	Jo, S., T. Kim, V. G. Iyer, and W. Im. 2008. CHARMM-GUI: a web-based graphical user interface for CHARMM. *J Comput Chem.* 29:1859-1865.
4.	Jo, S., J. B. Lim, J. B. Klauda, and W. Im. 2009. CHARMM-GUI Membrane Builder for mixed bilayers and its application to yeast membranes. *Biophys J.* 97:50-58.
5.	Lee, J., X. Cheng, J. M. Swails, M. S. Yeom, P. K. Eastman, J. A. Lemkul, S. Wei, J. Buckner, J. C. Jeong, Y. Qi, S. Jo, V. S. Pande, D. A. Case, C. L. Brooks, 3rd, A. D. MacKerell, Jr., J. B. Klauda, and W. Im. 2016. CHARMM-GUI Input Generator for NAMD, GROMACS, AMBER, OpenMM, and CHARMM/OpenMM Simulations Using the CHARMM36 Additive Force Field. *J Chem Theory Comput.* 12:405-413.
6.	Wu, E. L., X. Cheng, S. Jo, H. Rui, K. C. Song, E. M. Davila-Contreras, Y. Qi, J. Lee, V. Monje-Galvan, R. M. Venable, J. B. Klauda, and W. Im. 2014. CHARMM-GUI Membrane Builder toward realistic biological membrane simulations. *J Comput Chem.* 35:1997-2004.
7.	de Groot, J. C., K. Schluter, Y. Carius, C. Quedenau, D. Vingadassalom, J. Faix, S. M. Weiss, J. Reichelt, C. Standfuss-Gabisch, C. F. Lesser, J. M. Leong, D. W. Heinz, K. Bussow, and T. E. Stradal. 2011. Structural basis for complex formation between human IRSp53 and the translocated intimin receptor Tir of enterohemorrhagic E. coli. *Structure.* 19:1294-1306.
8.	Parrinello, M., and A. Rahman. 1981. Polymorphic Transitions in Single-Crystals - a New Molecular-Dynamics Method. *Journal of Applied Physics.* 52:7182-7190.
9.	Smit, B., and D. Frenkel. 2001. Understanding Molecular Simulation: From Algorithms to Applications. Elsevier.
10.	Best, R. B., X. Zhu, J. Shim, P. E. Lopes, J. Mittal, M. Feig, and A. D. Mackerell, Jr. 2012. Optimization of the additive CHARMM all-atom protein force field targeting improved sampling of the backbone phi, psi and side-chain chi(1) and chi(2) dihedral angles. *J Chem Theory Comput.* 8:3257-3273.
11.	Klauda, J. B., R. M. Venable, J. A. Freites, J. W. O'Connor, D. J. Tobias, C. Mondragon-Ramirez, I. Vorobyov, A. D. MacKerell, Jr., and R. W. Pastor. 2010. Update of the CHARMM all-atom additive force field for lipids: validation on six lipid types. *J Phys Chem B.* 114:7830-7843.
12.	MacKerell, A. D., D. Bashford, M. Bellott, R. L. Dunbrack, J. D. Evanseck, M. J. Field, S. Fischer, J. Gao, H. Guo, S. Ha, D. Joseph-McCarthy, L. Kuchnir, K. Kuczera, F. T. Lau, C. Mattos, S. Michnick, T. Ngo, D. T. Nguyen, B. Prodhom, W. E. Reiher, B. Roux, M. Schlenkrich, J. C. Smith, R. Stote, J. Straub, M. Watanabe, J. Wiorkiewicz-Kuczera, D. Yin, and M. Karplus. 1998. All-atom empirical potential for molecular modeling and dynamics studies of proteins. *J Phys Chem B.* 102:3586-3616.
13.	Zhang, Z., L. Lu, W. G. Noid, V. Krishna, J. Pfaendtner, and G. A. Voth. 2008. A systematic methodology for defining coarse-grained sites in large biomolecules. *Biophys J.* 95:5073-5083.

14.   Srivastava, A., and G. A. Voth. 2013. A Hybrid Approach for Highly Coarse-grained Lipid Bilayer Models. *J Chem Theory Comput.* 9:750-765.
15.   Lyman, E., J. Pfaendtner, and G. A. Voth. 2008. Systematic multiscale parameterization of heterogeneous elastic network models of proteins. *Biophys J.* 95:4183-4192.
16.   Allen, M. P., and D. J. Tildesley. 1989. Computer simulation of liquids. Clarendon Press, Oxford.
17.   Plimpton, S. 1995. Fast Parallel Algorithms for Short-Range Molecular Dynamics. *Journal of Computational Physics.* 117:1-19.
18.   Dunweg, B., and W. Paul. 1991. Brownian Dynamics Simulations without Gaussian Random Numbers. *International Journal of Modern Physics C.* 2:817-827.
19.   Davtyan, A., M. Simunovic, and G. A. Voth. 2017. The mesoscopic membrane with proteins (MesM-P) model. *The Journal of Chemical Physics.* 147:044101.
20.   Böckmann, R. A., A. Hac, T. Heimburg, and H. Grubmüller. 2003. Effect of Sodium Chloride on a Lipid Bilayer. *Biophysical Journal.* 85:1647-1655.
21.   Pandit, S. A., D. Bostick, and M. L. Berkowitz. 2003. Mixed Bilayer Containing Dipalmitoylphosphatidylcholine and Dipalmitoylphosphatidylserine: Lipid Complexation, Ion Binding, and Electrostatics. *Biophysical Journal.* 85:3120-3131.